PHYSICAL REVIEW E **94**, 051201(R) (2016)

Laser propagation measurements in long-scale-length underdense plasmas relevant to magnetized liner inertial fusion

A. J. Harvey-Thompson,[1] A. B. Sefkow,[1] M. S. Wei,[2] T. Nagayama,[1] E. M. Campbell,[3] B. E. Blue,[2] R. F. Heeter,[4] J. M. Koning,[4] K. J. Peterson,[1] and A. Schmitt[5]

[1]*Sandia National Laboratories, P.O. Box 5800, Albuquerque, New Mexico 87185, USA*

[2]*General Atomics, P.O. Box 85608, San Diego, California 92186, USA*

[3]*Laboratory for Laser Energetics, University of Rochester, Rochester, New York 14623-1299, USA*

[4]*Lawrence Livermore National Laboratories, P.O. Box 808, L-472, Livermore, California 94551, USA*

[5]*Naval Research Laboratory, Washington, DC 20375, USA*

(Received 5 July 2016; published 2 November 2016)

We report experimental results and simulations showing efficient laser energy coupling into plasmas at conditions relevant to the magnetized liner inertial fusion (MagLIF) concept. In MagLIF, to limit convergence and increase the hydrodynamic stability of the implosion, the fuel must be efficiently preheated. To determine the efficiency and physics of preheating by a laser, an Ar plasma with $n_e/n_{crit} \sim 0.04$ is irradiated by a multi-ns, multi-kJ, 0.35-μm, phase-plate-smoothed laser at spot-averaged intensities ranging from 1.0×10^{14} to 2.5×10^{14} W/cm^2 and pulse widths from 2 to 10 ns. Time-resolved x-ray images of the laser-heated plasma are compared to two-dimensional radiation-hydrodynamic simulations that show agreement with the propagating emission front, a comparison that constrains laser energy deposition to the plasma. The experiments show that long-pulse, modest-intensity ($I = 1.5 \times 10^{14}$ W/cm^2) beams can efficiently couple energy (~82% of the incident energy) to MagLIF-relevant long-length (9.5 mm) underdense plasmas. The demonstrated heating efficiency is significantly higher than is thought to have been achieved in early integrated MagLIF experiments [A. B. Sefkow *et al.*, Phys. Plasmas **21**, 072711 (2014)].

DOI: 10.1103/PhysRevE.94.051201

Recent experiments [1] have shown the magnetized liner inertial fusion (MagLIF) scheme [2,3] to be a promising route to achieving thermonuclear conditions in the laboratory. MagLIF implodes a cylindrical conducting liner, filled with a gaseous or cryogenically layered fusion fuel, in a *Z*-pinch configuration using a pulsed-power driver. The fuel is premagnetized by an externally applied axial magnetic field (10–30 T) and preheated using a high-power, long-pulse (2–10 ns) laser of moderate intensity (order 10^{14} W cm^{-2}) in order to reduce the implosion velocity and convergence requirements for reaching fusion-relevant plasma conditions. While the initial integrated MagLIF experiments confirmed laser preheat and premagnetization were necessary to achieve fusion conditions at stagnation, the fusion yield was approximately one order of magnitude lower than expected from detailed radiation-magneto-hydrodynamic (RMHD) simulations [3]. Subsequent experiments investigating the preheat efficacy suggested that the laser energy coupled to the gas was less than the simulations had predicted, which is thought to have been a major contributor to the lower than calculated yields. With this motivation, focused laser-preheating studies are now underway at a number of facilities to understand laser energy deposition at MagLIF-like conditions.

In the absence of laser-plasma instabilities (LPIs), laser energy deposition in MagLIF-relevant underdense plasmas proceeds via inverse-bremsstrahlung absorption balanced by hydrodynamic motion, thermal conduction, and radiative losses [4]. Previous experiments have been limited to small-scale (mm) experiments [5–8], or performed at high intensities [9], relevant to indirect-drive hohlraums which seek to minimize absorption in the gas with the latter potentially subject to significant nonlinear growth of LPIs. These experiments show that, when LPIs are not significant, RMHD codes such as HYDRA [5] can accurately model laser energy deposition [6,7]. However, at MagLIF-relevant scale lengths and parameters, there are no reported experiments to identify the target and drive conditions where undesirable LPIs become important, and thus hydrodynamic simulations have never been validated for MagLIF preheat physics.

In this Rapid Communication, temporally and spatially resolved measurements of laser energy deposition at MagLIF-relevant conditions are reported and compared to two-dimensional (2D) HYDRA [5] simulations. We present an experimental study of 0.35-μm laser energy deposition using beams of varying spot-averaged (750 μm diameter) intensities ($I = 1.0 - 2.5 \times 10^{14}$ W/cm^2) in unmagnetized, high-density (~1.7 mg/cm^3) Ar plasmas at scale lengths (10 mm), electron densities ($n_e \sim 0.038\, n_c$), laser pulse durations (2–10 ns), and $I\lambda^2$ values ($1.7-4.0 \times 10^{13}$ W cm^{-2} μm^2) relevant to MagLIF. The experiments provide important physical insight into MagLIF-relevant laser propagation and energy coupling over ~cm scale-length plasmas where hydrodynamic motion, thermal conduction, and radiation losses can be important. These results are compared with 2D simulations that show excellent agreement with the time-resolved beam propagation. The analysis indicates the amount of energy coupled into the gas within the 9.5-mm length of the targets is strongly dependent on the intensity of the beam, with a maximum energy coupled in excess of 80% of that delivered, a significantly higher fraction than is thought to have been achieved in early integrated MagLIF experiments [3].

The experiments were performed using the OMEGA-EP laser (0.351 μm, 3ω) at the Laboratory for Laser Energetics (LLE) using a gas-tube platform similar to that previously used to investigate laser heating of magnetized plasmas [8]. The cylindrical gas-tube targets, shown in Fig. 1(a), were

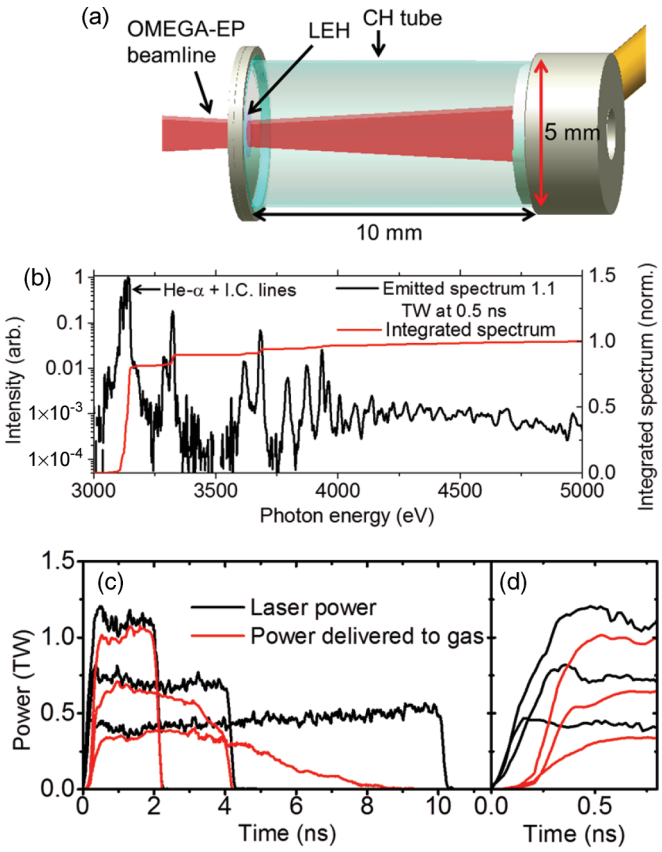

FIG. 1. (a) Experimental setup as viewed from the x-ray framing camera. (b) Measured x-ray spectrum taken at 0.5 ns into the 1.1 TW pulse showing the dominance of Ar *K*-shell emission. (c) Measured laser power (black) and inferred laser power deposited into the gas fill in simulations (red) for the three pulse shapes used; the early time behavior is highlighted in (d).

10-mm-long CH tubes, 5 mm in diameter, 75-μm wall thickness, filled with pure Ar gas that is contained at one end with a thin (1-μm-thick) polyimide laser entrance hole (LEH) window. The CH tube served as a surrogate for the metallic liner used in integrated MagLIF. It can hold high-pressure deuterium gas and is transparent ($\sim$50%) to $\sim 3-$ keV x rays. Ar was used instead of D_2 as the fill gas because it allows relevant absorption lengths to be obtained at low pressures, enables thin LEH windows, and emits diagnosable *K*-shell line radiation ($h\nu \sim 3$–4 keV) at the expected electron temperatures. The emission is dominated by the He-α and intercombination (I.C.) lines near 3.1 keV, as shown in Fig. 1(b). The targets were initially filled with 1 atm (14.7 psi) of pure Ar ($n_e \sim 4 \times 10^{20}\,\mathrm{cm}^{-3} \equiv 0.045\,n_c$ assuming average ionization, $\bar{Z} = 16$); however, the target pressure was not monitored immediately prior to the shots. Comparisons to simulations suggest the pressure may have dropped to 0.85 atm ($n_e \sim 3.4 \times 10^{20}\,\mathrm{cm}^{-3} \equiv 0.038\,n_c$) prior to the shots, a reasonable reduction in pressure. The value of n_e/n_c is similar to those used in early integrated MagLIF experiments ($n_e = 0.05\,n_c$) although the higher-Z ($\sim$16) Ar plasma will result in shorter absorption depths, more radiation emitted by the heated plasma, and more complex radiation physics. The same inverse-bremsstrahlung absorption physics

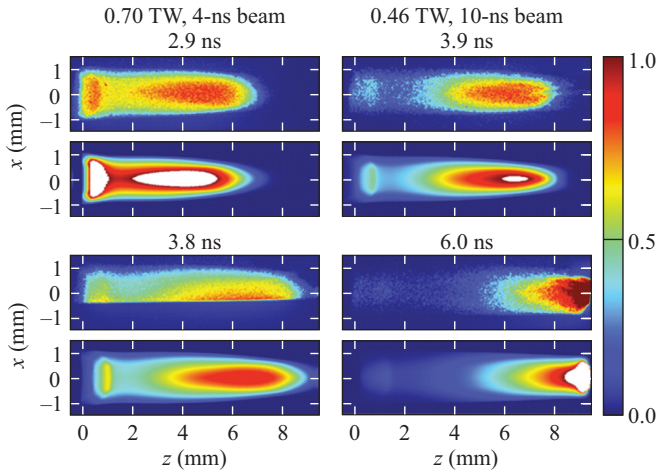

FIG. 2. X-ray framing camera images (top) and HYDRA simulations (bottom) for the 0.70 TW ($1.5 \times 10^{14}\,\mathrm{W/cm^2}$), and 0.46 TW ($1.0 \times 10^{14}\,\mathrm{W/cm^2}$) cases showing observed and simulated self-emission from the plasma. The time of the frame relative to the laser start time is indicated at the upper right corner of each picture. Regions above the estimated detector saturation threshold in simulations are marked in white. The bottom half of the 3.8 ns image for the 0.70 TW case is truncated due to misalignment of the detector.

should dominate energy coupling in both cases, however, making these experiments a valid test of laser absorption in RMHD codes albeit in a more complicated plasma and of laser preheat in MagLIF. The experiments were driven with a single OMEGA-EP beam focused with an $f/6.5$ lens that passed through the LEH window and propagated down the axis of the target. The driving beams were spatially smoothed with a distributed phase plate (DPP) to give a reproducible eighth order super-Gaussian, 750-μm-diameter spot (containing 95% of the beam energy). The propagations for three different beam powers were tested: 0.46, 0.70, and 1.1 TW with temporally square pulse lengths of 2, 4, and 10 ns, as shown in Fig. 1(c), corresponding to average intensities of 1.0, 1.5, and $2.4 \times 10^{14}\,\mathrm{W/cm^2}$, respectively. At these target and beam parameters deleterious LPIs, including scattering processes and filamentation, are not expected to be significant in the gas. During window disassembly, stimulated Brillouin scattering, two-plasmon decay, and stimulated Raman scattering instabilities may occur, though this is expected to only last $\sim$0.3 ns until the window plasma density is below $0.1 n_{crit}$. As a result, these processes should have negligible impact on the overall energy balance. The reproducible, well-defined spot profile together with accurate knowledge of the beam power (10% uncertainty), timing (0.1 ns), and LEH window thickness ($\sim$5%) means the majority of target and drive conditions were well known.

The extent of the heated plasma was imaged at multiple times during the laser pulse with a temporally (0.5 ns) and spatially ($\sim$0.1 mm) resolved four-frame x-ray framing camera (XRFC) filtered to view >3-keV photons, as shown in Fig. 2. The XRFC provides a field of view from the LEH window to 9.5 mm down the target. The LEH location is determined by the cutoff in intensity where emission is blocked by a washer that supports the LEH. The signal levels are proportional to the photons incident on the detector, but the response

becomes saturated in the regions of highest intensity on some of the images. Based on signal differences between cotimed frames recorded on the experiments and the x-ray spectroscopy [Fig. 1(b)], we estimate that there is an approximate factor of 2 relative uncertainty in the signal levels in regions where the detector is not saturated.

The experiments were modeled in 2D axisymmetry using the HYDRA code [5], which is a massively parallel, multiphysics, radiation-hydrodynamics design code that is used to model inertial confinement fusion and high-energy-density laboratory experiments, including early integrated MagLIF experiments [3]. The laser absorption model accounts for inverse-bremsstrahlung, refraction, and ponderomotive effects. Laser-plasma interaction processes such as stimulated Raman scattering, two-plasmon decay, and stimulated Brillouin scattering are not included in HYDRA, but as discussed above, are not expected to play a significant role in the laser-plasma coupling and energy balance. Electron thermal conduction is treated with multigroup flux-limited ($f = 0.05$) diffusion although reasonable variation (0.01–0.2) in the flux limiter does not significantly alter the results of these low-intensity experiments. Emitted radiation is modeled with an implicit Monte Carlo photonics transport package and non-local thermodynamic equilibrium detailed configuration accounting opacities [10] so that optical depth effects and mean-free-path effects are included.

Figure 2 shows synthetic XRFC images that include the instrument temporal and spatial response with the XRFC saturated region shown in white. The simulations use the measured beam power [Fig. 1(d)], spot profile, and target parameters, and assumes an Ar gas fill pressure of 0.85 atm for each experiment that is within the experimental uncertainty given the lack of *in situ*, shot-time measurement of the pressure. The simulated images match the axial and radial extent of the plasma at various times during the experiments for the three laser powers tested.

A comparison of axial lineouts at $r = 0$ averaged over the central ± 0.2 mm of the experimental and simulated XRFC images is shown in Fig. 3(a). While matching the data qualitatively, a quantitative comparison is not possible in regions where the detector is saturated. However, a quantitative comparison can be made at the leading edge of the emission where the detector response is not saturated and which simulations show is most sensitive to the energy deposited in the plasma. As shown in Fig. 3(b), the signal at the leading edge drops by an order of magnitude over ~ 0.5 mm in axial distance, and the factor of 2 in uncertainty in the peak intensity has a small effect when comparing the axial propagation.

As shown in Fig. 3(b), a consistent match to the data over an order of magnitude in signal level is found when assuming a gas fill pressure of 0.85 atm ($n_e = 3.4 \times 10^{20}\,\mathrm{cm}^{-3} \equiv 0.038\,n_c$) for all shots. At 1 atm, the location of the simulated emission front consistently lags that measured in all cases by 0.4–0.5 mm, a discrepancy outside of measurement errors. As discussed above, a 15% reduction in the fill pressure at shot time is reasonable and is considered the most plausible source for the discrepancy. Simulations suggest that experimental uncertainties in the LEH thickness (<0.1 micron) and beam power (<10%) do not contribute significantly to differences in the propagation velocity. To eliminate the pressure uncertainty

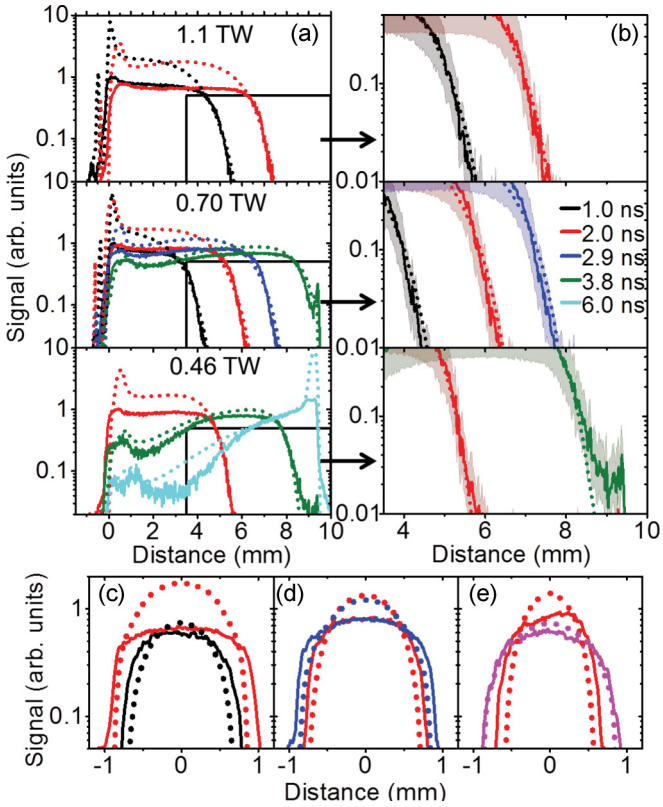

FIG. 3. (a) Comparison between experimental (solid) and simulated (dotted) axial profiles from Fig. 2 for the (top) 1.1 TW ($2.4 \times 10^{14}\,\mathrm{W/cm^2}$), (middle) 0.7 TW ($1.5 \times 10^{14}\,\mathrm{W/cm^2}$), and (bottom) 0.46 TW ($1.0 \times 10^{14}\,\mathrm{W/cm^2}$) cases averaged over the central 400-μm width. An expanded view of the leading edge of the propagation front for each case is shown in (b). The shaded region in (b) represents the factor of 2 error in measured signal level. Radial lineouts are shown for the (c) 1.1, (d) 0.70, and (e) 0.46 TW cases taken 4.0 mm down the target and averaged over ± 0.2 mm. Frame times use the same color coding throughout the figure.

at shot time, future experiments will use an *in situ* gas-pressure monitor.

Radial lineouts at $z = 4.0$ mm and averaged over ± 0.2 mm, shown in Figs. 3(c)–3(e), show that the simulated radial expansion of the emitting region matches that observed to within 0.12 mm. The agreement suggests that radial transport is well modeled and that there is little laser energy deposited or transported outside the original laser beam cone. As with the axial lineouts, the observed signal levels at the center where the emission is peaked are affected by detector saturation in some images, and in these regions a quantitative comparison between simulated and observed signal levels cannot be made. The agreement at the edges of the emission, however, where saturation does not occur are well matched by the modeling.

Figure 4(a) shows a plot of the measured and simulated axial emission-front distance as a function of time for the three shots. The emission-front distance is taken to be where the measured and simulated XRFC signals equal 0.1 of the peak in Fig. 3. The uncertainty in distance of 0.19–0.27 mm is derived from the combined factor of 2 estimated uncertainty that the measured peak signal levels' has in determining axial

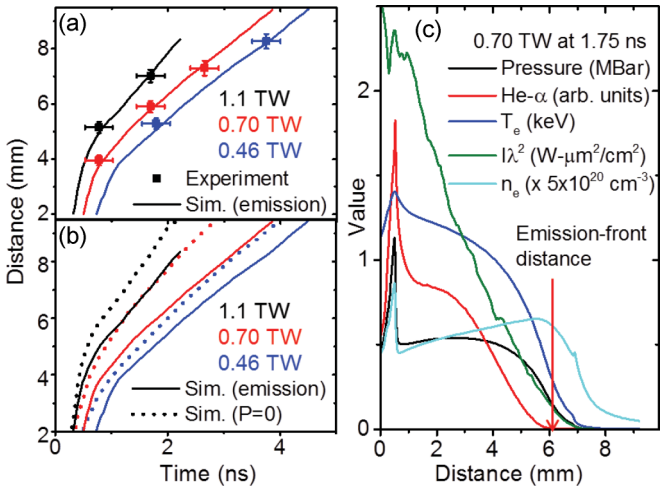

FIG. 4. (a) The measured and simulated axial emission-front distance as a function of time. Horizontal error bars on experimental data points represent the 0.5-ns XRFC integration time. (b) A comparison of the simulated axial emission-front distance and propagation distance defined as being where pressure = 0. (c) Axial lineouts of various quantities taken from a simulation of the 0.70 TW case at 1.75 ns.

distance (0.12–0.20 mm), the uncertainty in the magnification (2%), and the uncertainty in determining the LEH location (0.1 mm). The simulated lineouts in Fig. 4(c) show that the XRFC signal lags the true energy deposition front of the laser by about 1–2 mm since emission can only be observed for regions where $T_e \geqslant 500\,\mathrm{eV}$. The propagation distance vs time, where propagation distance is defined to be where simulated plasma pressure and $I\lambda^2$ drop to zero, is shown in Figure 4(b). The data and modeling reveal that higher laser intensity results in faster propagation velocity, as one would expect because it generates higher pressure. The simulations suggest there are broadly two spatial and temporal scales: depending on intensity, the first ~3–5 mm of laser penetration is more rapid with little energy (<10%) coupled, but for farther distances the velocity of the absorption front slows as energy is coupled more efficiently. The latter begins to occur when hydrodynamic motion and conduction losses slow the rate of absorption opacity loss as energy density is transported away from the center of the beam. This transport creates a density channel as the beam propagates, which prevents the beam cone from diverging with its original *f*-number (ratio of focal length to beam diameter) and confines the laser beam as it propagates down the tube. At the point where the propagation reaches the end of the target, the simulations calculate that the beams have coupled 1.8 kJ (1.1 TW, $2.4 \times 10^{14}\,\mathrm{W/cm^2}$), 1.6 kJ (0.70 TW, $1.5 \times 10^{14}\,\mathrm{W/cm^2}$), and 1.3 kJ (0.46 TW, $1.0 \times 10^{14}\,\mathrm{W/cm^2}$) to the plasma. The rapid propagation at early times in simulations is caused by the lack of appreciable hydrodynamic and conduction loss, as well as a small amount of energy being coupled to the gas from the laser and window during the LEH foil disassembly period. The laser penetrates to the far wall of the target after about 2–4 ns, depending on intensity, as shown in Fig. 4(b). Figures 1(c) and 1(d) show the power delivered to the gas as a function of time for the three pulse shapes. In the 1.1 TW case, almost all of the laser energy is absorbed in the gas. For the 0.7 TW and 0.46 TW cases the laser reaches the back wall late in time which quickly reduces the amount of energy coupled to the gas because most of the absorption per unit mass occurs near the deposition front. Furthermore, after about 3 ns, radiative losses from the hot argon plasma begin to become appreciable. The 0.7 TW case was only modestly affected, whereas the 0.46 TW case was dramatically affected by both striking the back wall and by radiation losses.

The results and simulations show the energy coupled into the plasma depends on the intensity, plasma density, and mean ion charge and the defined 10-mm target length, since absorption is balanced by hydrodynamic motion, thermal conduction, and radiation losses out of the laser path during its propagation through the plasma. In these experiments, ~1.6 kJ of laser energy (80% of the total energy) was deposited into the 9.5-mm-long gas at a modest spot-averaged intensity ($1.5 \times 10^{14}\,\mathrm{W/cm^2}$) and spot size (750 μm) over 3 ns and at a $\langle Z \rangle n_e^2/n_{crit}$ relevant for MagLIF. Future experiments will use a gas-pressure monitor and magnetized fusion fuel (deuterium) along with a planned backscatter-measurement diagnostic to further constrain experimental uncertainties and increase relevance to MagLIF.

The authors gratefully acknowledge the outstanding support of S. B. Hansen, C. A. Jennings, R. D. McBride, J. Emig, D. Canning, C. Sorce, V. Gelbov, C. Stoeckl, and the entire OMEGA-EP crew at the Laboratory for Laser Energetics and General Atomics for target fabrication. A.B.S. gratefully acknowledges M. M. Marinak, M. Pehul, and H. A. Scott for code support. Sandia is a multiprogram laboratory operated by Sandia Corporation, a Lockheed Martin Company, for the National Nuclear Security Administration under Contract No. DE-AC04-94AL85000. Support was also provided in part by the Laboratory Directed Research and Development Program at Sandia.

[1] M. R. Gomez, S. A. Slutz, A. B. Sefkow, D. B. Sinars, K. D. Hahn, S. B. Hansen, E. C. Harding, P. F. Knapp, P. F. Schmit, C. A. Jennings, T. J. Awe, M. Geissel, D. C. Rovang, G. A. Chandler, G. W. Cooper, M. E. Cuneo, A. J. Harvey-Thompson, M. C. Herrmann, M. H. Hess, O. Johns *et al.*, Experimental Demonstration of Fusion-Relevant Conditions in Magnetized Liner Inertial Fusion, Phys. Rev. Lett. **113**, 155003 (2014).

[2] S. A. Slutz, M. C. Herrmann, R. A. Vesey, A. B. Sefkow, D. B. Sinars, D. C. Rovang, K. J. Peterson, and M. E. Cuneo, Pulsed-power-driven cylindrical liner implosions of laser preheated fuel magnetized with an axial field, Phys. Plasmas **17**, 056303 (2010).

[3] A. B. Sefkow, S. A. Slutz, J. M. Koning, M. M. Marinak, K. J. Peterson, D. B. Sinars, and R. A. Vesey, Design of magnetized

liner inertial fusion experiments using the Z facility, Phys. Plasmas **21**, 072711 (2014).

[4] J. Denavit and D. W. Phillion, Laser ionization and heating of gas targets for long-scale-length instability experiments, Phys. Plasmas **1**, 1971 (1994).

[5] M. M. Marinak, G. D. Kerbel, N. A. Gentile, O. Jones, D. Munro, S. Pollaine, T. R. Dittrich, and S. W. Haan, Three-dimensional HYDRA simulations of National Ignition Facility targets, Phys. Plasmas **8**, 2275 (2001).

[6] N. B. Meezan, L. Divol, M. M. Marinak, G. D. Kerbel, L. J. Suter, R. M. Stevenson, G. E. Slark, and K. Oades, Hydrodynamics simulations of 2ω laser propagation in underdense gasbag plasmas, Phys. Plasmas **11**, 5573 (2004).

[7] D. H. Froula, L. Divol, N. B. Meezan, S. Dixit, J. D. Moody, P. Neumayer, B. B. Pollock, J. S. Ross, and S. H. Glenzer, Ideal Laser-Beam Propagation through High-Temperature Ignition Hohlraum Plasmas, Phys. Rev. Lett. **98**, 085001 (2007).

[8] A. J. Harvey-Thompson, A. B. Sefkow, T. N. Nagayama, M. S. Wei, E. M. Campbell, G. Fiksel, P.-Y. Chang, J. R. Davies, D. H. Barnak, V. Y. Glebov, P. Fitzsimmons, J. Fooks, and B. E. Blue, Diagnosing laser-preheated magnetized plasmas relevant to magnetized liner inertial fusion, Phys. Plasmas **22**, 122708 (2015).

[9] S. H. Glenzer, D. H. Froula, L. Divol, M. Dorr, R. L. Berger, S. Dixit, B. A. Hammel, C. Haynam, J. A. Hittinger, J. P. Holder, O. S. Jones, D. H. Kalantar, O. L. Landen, A. B. Langdon, S. Langer, B. J. MacGowan, A. J. MacKinnon, N. Meezan, E. I. Moses, C. Niemann *et al.*, Experiments and multiscale simulations of laser propagation through ignition-scale plasmas, Nat. Phys. **3**, 716 (2007).

[10] H. A. Scott and S. B. Hansen, Advances in NLTE modeling for integrated simulations, High Energy Density Phys. **6**, 39 (2010).